The Astrophysical Journal Supplement Series, 278:1 (14pp), 2025 May https://doi.org/10.3847/1538-4365/adc451

15 yr of Interstellar Neutral Hydrogen Observed with the Interstellar Boundary Explorer

André Galli[1], Paweł Swaczyna[2], Maciej Bzowski[2], Marzena A. Kubiak[2], Izabela Kowalska-Leszczynska[2], Peter Wurz[1], Fatemeh Rahmanifard[3], Nathan A. Schwadron[3], Eberhard Möbius[3], Stephen A. Fuselier[4,5], Justyna M. Sokół[4], Jonathan Gasser[4], Jacob Heerikhuisen[6], and David J. McComas[7]

[1] Space Science and Planetology, Physics Institute, University of Bern, Bern, Switzerland; andre.galli@unibe.ch
[2] Space Research Centre PAS (CBK PAN), Warsaw, Poland
[3] University of New Hampshire, Durham, NH, USA
[4] Southwest Research Institute, San Antonio, TX, USA
[5] University of Texas at San Antonio, San Antonio, TX, USA
[6] Department of Mathematics and Statistics, University of Waikato, Hamilton, New Zealand
[7] Department of Astrophysical Sciences, Princeton University, Princeton, NJ, USA
Received 2025 January 31; revised 2025 March 14; accepted 2025 March 19; published 2025 April 14

Abstract

The interactions of our heliosphere with the surrounding local interstellar medium (LISM) lead to a range of observable phenomena such as energetic neutral atoms (ENAs) from the boundary regions of the heliosphere and the influx of interstellar neutrals (ISNs) into the inner solar system. Hydrogen is the dominant neutral species in the LISM, but due to ionization and radiation pressure, only a fraction of the ISN H atoms reach the inner solar system close to Earth. Monitoring this signal therefore provides observational constraints on our assumptions of the LISM and the solar-activity-dependent loss processes inside the heliosphere. The IBEX-Lo instrument on board the Interstellar Boundary Explorer has been the only instrument so far to measure ISN H atoms directly, together with ISN D, He, Ne, O, and ENAs in the energy range from tens of eV to 2 keV. This study covers 15 yr of IBEX-Lo ISN H observations, i.e., more than one solar cycle and includes two solar minima when the ISN H signal in IBEX-Lo is strongest. Despite the very intense ISN He signal, the ISN H signal can be retrieved with appropriate knowledge of the instrument, choice of optimum observation season, and supporting modeling. The retrieved ISN H signal shows a clear anticorrelation with solar activity. The resulting ISN H maps are available in orbit format and in ecliptic coordinates and will be the basis for future more detailed comparison with heliosphere models.

Unified Astronomy Thesaurus concepts: Heliosphere (711); Heliosheath (710); Interstellar medium (847); Interstellar atomic gas (833); Solar cycle (1487)

Materials only available in the online version of record: data behind figures

1. Introduction

The heliosphere is defined as the region in outer space dominated by the solar wind. This region is constrained by the surrounding local interstellar medium (LISM). In the unperturbed LISM, hydrogen is the dominant interstellar neutral (ISN) species whereas in the inner solar system (at heliocentric distances of a few astronomical units or less), ISN helium dominates (J. M. Sokół et al. 2019, e.g.,). This change is caused by ionization losses inside the heliosphere and radiation pressure that act much more strongly on H than on He. Depending on solar radiation (which varies with solar activity), only a fraction of the ISN H atoms reach the inner solar system close to Earth. This fraction is much smaller than that of interstellar He. Ionization losses and radiation pressure act stronger on slower atoms within the population of interstellar H, which changes the distribution at 1 au in favor of faster H atoms (M. Bzowski et al. 1997). The measured ISN H signal therefore provides constraints to our understanding of solar-activity-dependent loss processes inside the heliosphere and on the properties of the interstellar medium. In contrast to He, ISN H atoms at 1 au are believed to be mostly secondary atoms originating around the heliopause (M. A. Kubiak et al. 2024). The differentiation between the primary and secondary H populations from measurements at 1 au is only possible through modeling support.

The Interstellar Boundary Explorer (IBEX) is a NASA small explorer mission, placed in a high-altitude Earth orbit (D. J. McComas et al. 2009, 2011). IBEX carries two scientific instruments: IBEX-Hi (H. O. Funsten et al. 2009a) and IBEX-Lo (S. A. Fuselier et al. 2009b). Since its launch in 2008, IBEX has successfully measured ISN H, D, He, Ne, and O, as well as energetic neutral atoms (ENAs) from the heliosphere boundary regions in the energy range from tens of eV to 6 keV with the two instruments IBEX-Lo and IBEX-Hi (see e.g., H. O. Funsten et al. 2009b; S. A. Fuselier et al. 2009a; D. J. McComas et al. 2009, 2024; E. Möbius et al. 2009, 2012; N. A. Schwadron et al. 2009; P. Bochsler et al. 2012; D. F. Rodríguez Moreno et al. 2013; J. Park et al. 2019; A. Galli et al. 2022a, 2022b).

This study presents a comprehensive set of maps of ISN H observed with IBEX-Lo from 2008 December until 2023 April. This is a follow-on to the study by A. Galli et al. (2019), covering 15 yr including two solar minima. Solar minima offer the best opportunity to detect the ISN H signal in the inner heliosphere because the ISN H loss processes are weakest (L. Saul et al. 2013; N. A. Schwadron et al. 2013; O. A. Katushkina et al. 2015, 2021; F. Rahmanifard et al. 2019).

A fraction of the incoming neutral H atoms are converted on the conversion surface of IBEX-Lo to H^- and subsequently analyzed with an electrostatic analyzer and a time-of-flight (TOF) mass spectrometer. However, H^- count rates can also be

Table 1
The Data Selected for This Study

Season	Dates	PAC Voltage	Energy Steps	Orbits
1	2008 Dec–2009 Jun	Nominal	Normal (1-2-3-4-5-6-7-8)	11–31
2	2009 Oct–2010 Jun	Nominal	Normal	49–80
3	2010 Nov–2011 Jun	Nominal	Normal	102–127
4	2011 Nov–2012 Jun	Nominal	Normal	145a–169b
5	2012 Oct–2013 Jun	Lowered	Normal	183a–209b
6	2013 Oct–2014 Jun	Lowered	Normal	223a–249b
7	2014 Oct–2015 Jun	Lowered	Normal	262a–288b
8	2015 Oct–2016 Jun	Lowered	Normal and 1-1-2-2-5-6-7-8	305a–328b
9	2016 Sep–2017 May	Lowered	Normal and 1-1-2-2-3-6-7-8	340a–367b
10	2017 Sep–2018 May	Lowered	Normal and 1-1-2-2-3-6-7-8	381a–407b
11	**2018 Sep–2019 May**	Lowered	Normal and 1-1-2-2-3-6-7-8	**419a–447b**
12	**2019 Sep–2020 May**	Lowered	Normal and 1-1-2-2-3-6-7-8	**461a–485b**
13	**2020 Sep–2021 May**	Lowered	Normal and 1-1-2-2-3-6-7-8	**501a–527b**
14	**2021 Sep–2022 Apr**	Lowered	Normal and 1-1-2-2-3-6-7-8	**541a–564b**
15	**2022 Sep–2023 Apr**	Lowered	Normal and 1-1-2-3-4-6-7-8 and 1-1-2-2-3-6-7-8	**581a–603b**

Note. Printed in bold are the new seasons not covered by A. Galli et al. (2019).

caused by ISN He (via sputtering of H^- off the conversion surface) and to a much lesser extent by heliospheric ENAs (A. Galli et al. 2019) and other sources. We therefore use a bootstrap method to subtract the H^- count rates caused by ISN He from the signal caused by ISN H. The parameters required to subtract the ISN He contribution were derived in two different ways to assess how sensitive the resulting ISN H maps are to model assumptions.

In the following sections, we will first describe the data selection process (Section 2) and give details on the ISN H retrieval method and its uncertainties (Section 3). This description is followed by a comprehensive results section with ISN H maps of all 15 yr plus time-series and map cross sections (Section 4) and by the conclusions in Section 5.

2. Data Set

Because of their low energies, ISN H atoms arriving at IBEX only fall in the two lowest energy bins of IBEX-Lo. For this study, we use the H^- count rates measured in the three lowest energy bins with central energies at 15, 29, and 55 eV of IBEX-Lo. Energy bin 3 is required to derive ISN H contributions in energy bins 1 and 2 because count rates in energy bin 3 are a measure of the ISN He signal without ISN H contribution. The dates covered by our data set are shown in Table 1. The first orbits per season (e.g., orbits 49–53 in the second season) often contain only antiram observations and are therefore only used to estimate background levels. In 2012 July, the postacceleration voltage of the TOF detector had to be lowered from 16 to 7 kV, which led to a decrease in detection efficiency (A. Galli et al. 2019). Observation times with special instrument settings where energy bins 1, 2, and 3 were not acquired were omitted from this study (orbits 537–539 and 575–580 in magnetosphere mode, see Table 1).

The time selection process for this new study is identical to the process chosen by A. Galli et al. (2019) to maintain backward compatibility: the general GoodTimes list serves as the starting point. This list is culled with the requirements that (a) the number of counts is <4 per hemisphere in energy bins 7 and 8 and (b) that the TOF2 count rate at a given time be less than 1.6 times the minimum TOF2 count rate encountered during the orbit under consideration. We verified that our data selection reproduced the H^- count-rate maps for the years 2009–2018 prepared and released by A. Galli et al. (2019) and then applied the same selection process to the five additional ISN seasons 2019–2023.

Figure 1 shows one of these raw H^- count-rate maps, i.e., ISN season 2 from 2009 October–2010 June, orbits 49 to 80, energy bin 1. The color code represents the rate in counts per second, and white pixels indicate no data (such as in orbit 62). ISN atoms are only observed in the ram hemisphere; the antiram hemisphere features very low count rates because of the low energies and fluxes. The only obvious exception is the electronics-related count rates at one constant spin angle. The sequence of different ISN signals seen in the ram hemisphere is representative for all seasons, but the ISN H signal in this season was considerably stronger than in years of high solar activity: the ISN He secondary signal (the Warm Breeze; M. A. Kubiak et al. 2014) is followed by the primary ISN He with peak count rates reaching tens of counts per second, and finally by the main ISN H signal. The blue pixels around orbit 70 correspond to 1 count s^{-1} at most.

3. Retrieval Methods

Relying on the H^- count-rate maps in energy bins 1, 2, and 3, we retrieved the contribution from ISN H in the two lowest energy bins 1 and 2. The H^- count-rate maps are dominated by H^- generated by ISN He. These H^- counts emerge as sputter products from the conversion surface, while incoming ISN H produces, to a lesser extent, converted H^- on the conversion surface. However, two weak (compared to the ISN signals) background contributions must be considered in addition: a ubiquitous background (A. Galli et al. 2015, 2017) and all other background sources that may vary with space and time: heliospheric ENAs, magnetospheric contamination, and H^- sputtered by ISN Ne and O. We use the same approach of a bootstrap method as in A. Galli et al. (2019), going from higher to lower energies, to subtract the count rates from ISN He and from other background sources to derive the underlying ISN H.

3.1. Bootstrap Equations to Calculate ISN H from Measured Count Rates

Explicitly, the ISN H integral intensity J in units of cm^{-2} sr^{-1} s^{-1} in energy bin 2 for map pixel i, j is calculated from the

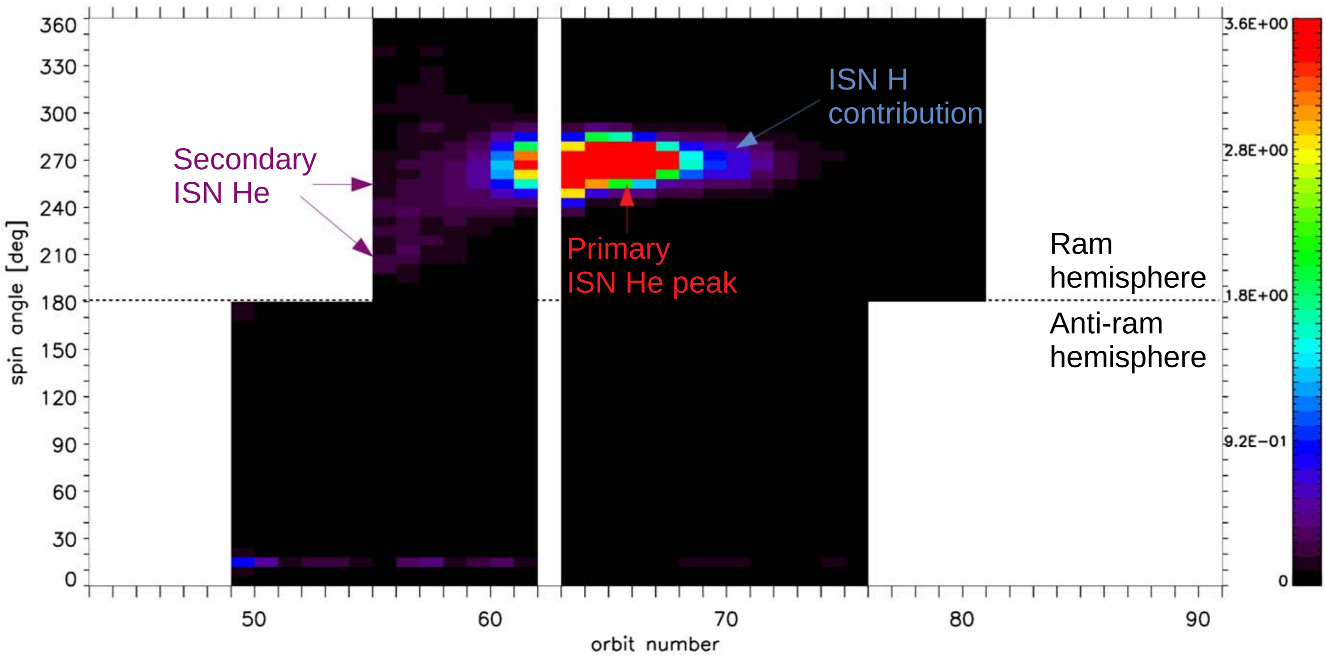

Figure 1. Map of raw H^- in units of counts per second for energy bin 1 of ISN season 2. The upper 30 spin angles correspond to the ram hemisphere, the lower spin angles correspond to the antiram hemisphere of IBEX-Lo observations. The band of count rates at 15° spin angle is an electronics artifact. These count-rate maps are the basis to separate the ISN H signal (visible as blue pixels around orbit 70) from the count rates due to primary and secondary ISN He. No data were acquired during orbit 62.

measured H^- count rates $c(2)$ and $c(3)$ in energy bins 2 and 3 as

$$J(2)_{i,j} = \frac{[c(2)_{i,j} - bg(2)_i] - \alpha(23)_{i,j}[c(3)_{i,j} - bg(3)_i]}{G(22)}. \quad (1)$$

In the above equation, the average background rates for that specific orbit i, $bg(2)_i$ and $bg(3)_i$, are calculated as an average over the antiram hemisphere of said orbit. This is based on the knowledge that ISN signals are not energetic and intense enough to ever be measurable in the antiram direction (A. Galli et al. 2015). Using antiram hemisphere count rates as measure of all background and ENA signals is accurate for any local background produced in the rest frame of the spacecraft or the Earth. Because of the Compton–Getting effect this approach may underestimate the ENA contribution, but that contribution is typically on the order of the ubiquitous count rate of roughly $0.01\ s^{-1}$ (A. Galli et al. 2014). This is 2 orders of magnitude lower than the count rate measured for the ISN H signal during peak season (roughly $1\ \mathrm{count\ s}^{-1}$ for orbit 70 in the ecliptic plane, see Figure 1). The energy-dependent ratio $\alpha(23)_{i,j}$ defines how many H^- counts are produced in energy bin 2 compared to energy bin 3 by an incoming ISN He at a given energy, sputtering H^- from the instrument conversion surface. The conversion factor $G(22)$ is a constant determined from laboratory calibration and converts the calculated count rates in energy bin 2 into integral intensity in energy bin 2. In analogy, the subsequent equation to calculate the ISN H integral intensity J in energy bin 1 for map pixel i, j is calculated from the measured H^- count rates $c(1)$ and $c(3)$ in energy bins 1 and 3 as

$$J(1)_{i,j} = \frac{[c(1)_{i,j} - bg(1)_i] - \alpha(13)_{i,j}[c(3)_{i,j} - bg(3)_i] - [G(21)J(2)_{i,j}]}{G(11)}. \quad (2)$$

Equation (2) is analogous to Equation (1) except for the subtraction of the expected contribution of H^- into the lower energy bin 1 from H atoms at higher energies. This corresponds to a relative change in derived $J(1)$ of maximum 10% for most pixels. The complete list of G-conversion factors is compiled in Table 2. The relative uncertainty of these conversion factors is assumed to be 30% in accordance with the uncertainty of IBEX-Lo laboratory calibration (S. A. Fuselier et al. 2009b).

Table 2
Conversion Factors Based on Laboratory Calibration to Convert H^- Count Rates into Integral Intensity (see Equations (1) and (2))

Conversion Factor (cm^2 sr eV eV^{-1})	Before 2012 June	After 2012 June
$G(22)$	$0.93 \times 1.41 \times 10^{-5}$	$0.435 \times 1.41 \times 10^{-5}$
$G(21)$	$0.93 \times 4.23 \times 10^{-6}$	$0.435 \times 4.23 \times 10^{-6}$
$G(11)$	$0.93 \times 7.29 \times 10^{-6}$	$0.434 \times 7.29 \times 10^{-6}$

Note. The middle column is before 2012 June, the right column is after 2012 June (when the postacceleration and the throughput of IBEX-Lo were lowered).

Given the low background count rates (on the order of $0.01\ s^{-1}$) compared to the count rates caused by ISN He and ISN H (on the order of $1\ s^{-1}$), the most important parameters in Equations (1) and (2) are the α-parameters required for the subtraction of the intense ISN He signal. For this study, we used by default the so-called in-flight calibration approach ("H3_inflight" in A. Galli et al. 2019, see details in the next subsection) to derive these α-parameters. In addition, we considered a simplistic alternative where all α-parameters were set to 1.0 to verify the in-flight approach.

3.2. Derivation of In-flight Parameters for the Instrument Response to ISN He

The derivation of the in-flight α-parameters in Equations (1) and (2) is based on the work by P. Swaczyna et al. (2023): The authors derived the IBEX-Lo in-flight relative response based

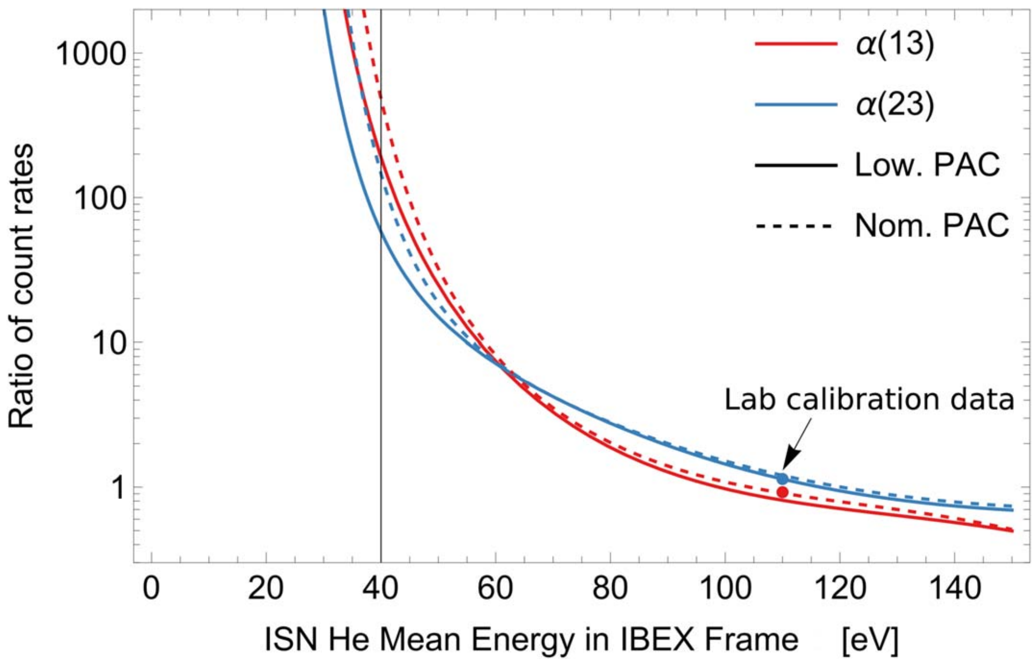

Figure 2. Expected ratios of ISN He count rates in energy bin 1 to bin 3 ($\alpha(13)$) and in energy bin 2 to bin 3 ($\alpha(23)$) as a function of the mean energy of incoming ISN He atoms. The solid and dashed lines (in blue or red) correspond to the nominal and lower PAC voltages, respectively. The two laboratory calibration data points are shown as dots. We adopt a somewhat arbitrary limit at 40 eV, below which the response in energy bin 3 is too low to provide the basis for this analysis.

on the ISN observations supported with modeling of the ISN He energy in the IBEX reference frame. The mean energy in each pixel was calculated from the comprehensive model of ISN He, combining both the primary and secondary populations. The model utilizes the global heliosphere model (E. J. Zirnstein et al. 2016; J. Heerikhuisen et al. 2019) to calculate the charge-exchange filtration of ISN He atoms with the methodology presented by M. Bzowski et al. (2017, 2019). Compared to the three-dimensional model of ISN He velocity distribution functions throughout the heliosphere by F. Fraternale et al. (2021), the approach by P. Swaczyna et al. (2023) relied on a very specific two-dimensional projection of the distribution function to just derive the ISN He mean energy at the IBEX position.

Figure 2 shows the ratio of H^- count rates in IBEX-Lo caused by ISN He, i.e., the $\alpha(13)$ and $\alpha(23)$ parameters used in Equations (1) and (2). For He at 110 eV energy, ratios from laboratory calibration also exist. These values of $\alpha(23) = 1.16$ and $\alpha(13) = 0.94$ are overplotted as dots in Figure 2 and match the in-flight parameters at this energy. The calculated parameters increase for lower energies due to the decreasing probability of measuring ISN He atoms in energy bin 3. We chose the energy limit at 40 eV, below which the signal expected in bin 3 is too low for analysis. Nevertheless, even for energies slightly above the limit, the resulting uncertainty of the procedure is typically too high to provide a robust data point due to the multiplication of the count-rate uncertainty in energy bin 3 by this large factor. While the methodology uses the mean energy of ISN He from the modeling, the details of the models do not affect the mean energy (see discussion in P. Swaczyna et al. 2023). Therefore, while the current analysis is not fully model-free, the impact of the models is rather limited. This is confirmed by the comparison of the ISN H maps resulting from the in-flight approach and from a simplistic approach with uniform α (see Section 4.1).

Until orbit 167 in 2012 June, the IBEX-Lo observations were affected by unintended data losses in the instrument's buffer. A high rate of events caused by electrons may exceed the maximum throughput of the buffer and thus throttle the buffer. P. Swaczyna et al. (2015) developed a detailed model of these losses to estimate a correction factor compensating for these losses. The relative response found by P. Swaczyna et al. (2023) used the throughput-corrected data. However, this study relies on raw count rates, and the correction factor must be implemented separately. These correction factors are 1.067 ± 0.015, 1.110 ± 0.027, and 1.24 ± 0.09 for energy bins 1, 2, and 3, respectively. The uncertainty represents the orbit-to-orbit variability. The α-parameters were therefore adjusted to account for this throttling effect: $\alpha(13)$ was multiplied by 1.17 ± 0.09 and $\alpha(23)$ by 1.12 ± 0.09 for the data collected until orbit 167. The event selection logic of the sensor was changed starting with orbit 168 to eliminate a high load of electron events, preventing the buffer throttling and thus the need for this correction.

3.3. Uniform Parameters for the ISN He Instrument Response for Comparison

To check the sensitivity of the ISN H retrieval method on the in-flight parameters presented in the previous subsection, we also set up a simplistic approach to derive the α-parameters: The equations to derive ISN H remain identical to Equations (1) and (2), but constant α parameters were used instead. We tested two variants, either using the laboratory constants for 110 eV ISN He ($\alpha(13) = 0.94$, $\alpha(23) = 1.16$) shown in Figure 2 or just assuming $\alpha \equiv 1$ for both parameters everywhere. These two variants do not differ significantly from each other as we estimate a relative uncertainty of 30% for these constant α-parameters in any case (see next subsection). Moreover, both variants overlap with the in-flight approach for spin angles close to the ecliptic plane where the ISN H signal

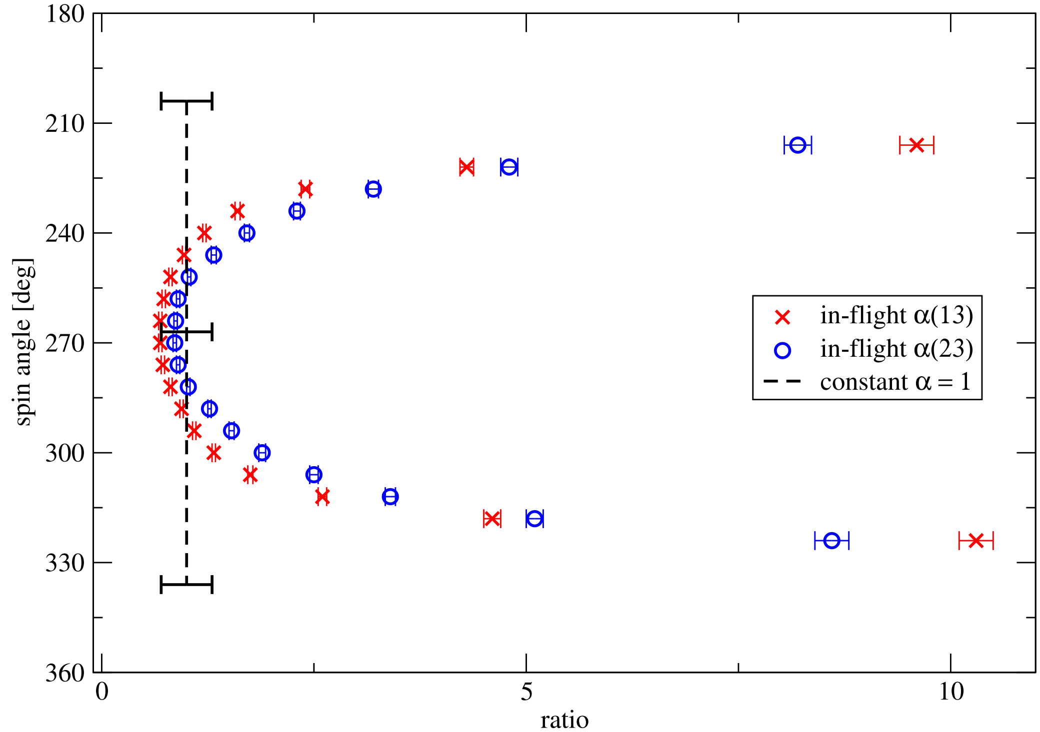

Figure 3. Ratio of H^- count rates caused by ISN He in IBEX-Lo energy bins 1, 2, and 3 plotted against IBEX-Lo spin angle (180° ≃ ecliptic north pole, 270° ≃ ecliptic plane) for the example of orbit 70. The $\alpha(13)$ and $\alpha(23)$ values are based on the in-flight approach, thus depending on ISN He energy and ecliptic latitude; the simplistic approach assumes constant α values everywhere.

usually appears. This is illustrated in Figure 3 for the example of orbit 70 in ISN season 2010: the α-parameters are plotted over the spin angles of the ram hemisphere covered with IBEX-Lo. Spin angle 180° corresponds to the ecliptic north pole if the IBEX spin axis is directly pointing to the sunward direction and thus spin angle 270° corresponds to the ecliptic plane. To see the effect of the different approaches on retrieved ISN H, we chose the approach with $\alpha = 1 \pm 0.3$ and juxtaposed it to the results obtained with the default in-flight α-parameters (see Section 4.1).

The comparison of the ISN H maps derived with the two different approaches demonstrates the impact of these assumptions, i.e., for which regions the derived ISN H intensities depend on our assumptions for the ISN He sputter products. In Section 4.1, we show a specific example for an ISN H map derived with $\alpha \equiv 1$.

3.4. Uncertainties

The uncertainties of the derived ISN H intensities in Equations (1) and (2), σ_{J2} and σ_{J1}, are calculated by error propagation of uncorrelated error sources, i.e., as the quadratic sum of all error contributions. The individual errors are estimated to be 30% for all $G(**)$-factors and the standard deviation of the average is used as measure of uncertainty of background levels $bg(*)$. For the count rates $c(*)$, the sum of the statistical error (assuming a Poisson distribution with counts divided by the exposure time t_{expo}, which can vary between 135 s and 574 s with solar cycle and energy stepping modes specified in Table 1) plus the systematic error (caused by weak background sources, heliospheric ENAs, magnetospheric contamination, etc.) is used, i.e.,

$$\sigma_{c(*)_{i,j}} = \sqrt{s^2 + c(*)_{i,j}/t_{\mathrm{expo}}};$$
$$s = 0.01\ \mathrm{s}^{-1}\ \text{before 2012 June and}\ s = 0.005\ \mathrm{s}^{-1}\ \text{afterward.} \tag{3}$$

Finally, for the α-parameters, a relative error of 2% is assumed for the default approach after 2012 June. Before that date, the buffer throughput was corrected for via adjusting the in-flight α-parameters (see Section 3.2), but this correction introduced an additional uncertainty: the relative uncertainty before 2012 June therefore is 9.3% for $\alpha(13)$ and $\alpha(23)$. For the approach with constant α-parameters (Section 3.3), the same relative uncertainty of 30% as for the laboratory calibration $G(^{**})$-factors is assumed.

4. Results

We applied Equations (1) and (2) for both α-parameter approaches to the count-rate maps (as shown in Figure 1) to retrieve ISN H flux maps in energy bins 1 and 2 for each of the 15 seasons. The main challenge for these retrievals turned out to be the regions where the intense ISN He signal overlaps with the ISN H signal. We first present the comparison of the two α-parameter approaches before showing the main results of all ISN H maps for the default retrieval and discussing the time series of the ISN H fluxes over the entire 15 yr.

4.1. Comparison of Retrieval Approaches

We first verified that the simplistic approach with constant α-parameters reproduces the ISN H maps produced with the "H3_lab" approach for the years 2009–2018 (A. Galli et al. 2019) if the identical constants are used.

Next, we verified that assumptions on ISN He and other model assumptions do not bias the resulting ISN H maps, since the maps should provide constraints to models rather than depend on them. As a study case, we chose the season of 2009–2010: Figure 4 shows the maps of ISN H intensities (left column) and their corresponding relative uncertainties (right column) for energy bins 1 (top rows) and 2 (bottom rows). The map format shows pixels plotted in a rectangular grid with orbit numbers per season as the *x*-axes and the 30 spin angles of the ram hemisphere for a given orbit as the *y*-axes. The top pixel rows correspond to the ecliptic north pole, the bottom pixel rows correspond to the ecliptic south pole. The first and third rows of plots in Figure 4 show the default approach with in-flight α-parameters for ISN He subtraction depending on individual pixels and orbits, whereas the second and fourth rows of plots were derived with $\alpha \equiv 1$.

Generally, the ISN H maps derived with the different α-parameters look similar to each other. In particular, the regions of reliable and strong ISN H signals in energy bin 1 close to the ecliptic plane with relative uncertainties typically 30% (blue blobs in upper right panels of Figure 4) are almost identical. Here, the ISN H signal was close to its peak whereas the ISN He peak signal around orbit 64 had already passed. The main challenge for retrieving ISN H is the overlying ISN He signal: the count rates caused by the ISN He peak reached almost 20 s^{-1} in contrast with the $\leqslant 1\ s^{-1}$ due to ISN H (see Figure 1). Therefore, the derived ISN H signal earlier in the year (orbits 63–68) differs between the different methods and the relative uncertainty of the derived intensity is larger than the intensity itself. For higher energies (bottom panels), we realize that for latitudes closer to the poles where ISN He energies are smaller and α-parameters increase rapidly, the differences in retrieved ISN H also increase. The approach with $\alpha \equiv 1$ turns out to be too simplistic at latitudes close to the poles. For instance, the red streak of intensities derived with $\alpha \equiv 1$ in energy bin 2 (see the bottom left panel of Figure 4) is not reproduced with the more refined in-flight approach.

The total error of retrieved ISN H intensities $J(^{*})$ is dominated by σ_c and σ_α. The main reason for the small discrepancies between the ISN H maps in Figure 4 close to the ecliptic plane is therefore the assumed relative uncertainty of the α-parameters (30% compared to only a few percent for the in-flight parameters). As a consequence, the ISN H maps derived with the in-flight parameters tend to show more pixels (in particular underlying the strong ISN He prime signal) that are considered reliable, i.e., with a relative uncertainty smaller than 1.0.

This is illustrated by the results in Figure 5 where the retrieved ISN H intensities are plotted versus orbit number, corresponding to a cross section of the ISN H map in ecliptic longitude. During the ISN He peak season around orbit 64 (E. Möbius et al. 2012), the derived ISN H intensities in energy bins 1 and 2 differ to some extent depending on the approach. However, these differences are not significant because of the large error bars of several $10^5\ cm^{-2}\ sr^{-1}\ s^{-1}$. Both approaches agree in that orbit 69 saw the highest ISN H intensity in energy bin 1. Later in the ISN season (orbits 69–80 in 2010), the ISN He peak signal has passed and mostly ISN H is left. As a result, the retrieved ISN H is well constrained (relative uncertainties typically of the order of 30%) and almost independent of the assumed α-parameters. A similar result is obtained for derived ISN H intensities versus spin angle, corresponding to a latitudinal cross section at orbit 70 (Figure 6). The retrieval results are identical within error bars. The main benefit of the in-flight approach are the smaller error bars in the presence of a strong ISN He signal. In Figures 5 and 6, red symbols denote results from the in-flight approach and black symbols show results from the more simplistic approach with $\alpha \equiv 1$. Since the latitudinal cross section was chosen for an orbit where total H^- count rates are dominated by the ISN H contribution, the retrieved ISN H intensities are almost identical between the different approaches (compare the red and black lines in Figure 6).

4.2. Overview of Maps for All 15 Seasons

Because of the expansion of the longitudinal validity range of the ISN H retrieval and the improved uncertainties with the in-flight calibration approach, we derived ISN H maps with the in-flight approach for energy bins 1 and 2 for all 15 yr in analogy to the first and third row of Figure 4. For future analyses relying on a quantitative comparison with heliosphere models in analogy to F. Rahmanifard et al. (2019) and O. A. Katushkina et al. (2021), the original map format with IBEX orbit and spin angle is preferable because remapping the data into another map frame may introduce aliasing effects due to averaging over map pixels. For a quick interannual comparison, however, it is very useful to plot the annual ISN H maps in ecliptic longitude and latitude.

To this end, we translated the spin angle and orbit of the original map format into ecliptic coordinates, relying on the IBEX-Lo pointing directions from the IBEX database at https://ibex.princeton.edu/RawDataReleases. For each orbit, the median longitude was taken as the pixel-center longitude for all pixels of the respective orbit. Similarly, for each season the pixel-center latitudes were averaged over all orbits. Pixel boundaries were set at the middle between neighboring bin centers. This resulted in continuous maps without overlap and without the need to rebin measured intensities. The resulting mapping inaccuracy is $<0\overset{\circ}{.}5$ in the relevant ecliptic latitude range.

Figure 7 shows as an example the retrieved ISN H maps for the season 2009–2010 (first and third row from Figure 4) transformed into a Mollweide projection in ecliptic coordinates. This map, like all subsequent Mollweide maps, is centered on the approximate heliospheric upwind direction, i.e., $\lambda_{ecl} = 255^\circ$ and $\beta_{ecl} = +5^\circ$ (D. J. McComas et al. 2015). Note that the longitude values decrease from left to right in the Mollweide maps. This is in accordance with the usual convention for sky maps and with previous ecliptic maps of IBEX data, but it is opposite to the sequence in the orbit versus spin-angle format where time and ecliptic longitude increase from left to right.

Figures 8–10 show the full sequence of retrieved ISN H in energy bin 1 in a Mollweide projection from 2009 to 2023. The color scale of intensities in the left columns is identical for all 15 plots, and the right columns show the corresponding relative uncertainty of the intensities (σ/J). The maximum ISN H signal appears in the years around solar minimum in 2009 and 2020. The signal becomes weaker and the spatial distribution becomes patchy during solar maximum from 2012 to 2016 and from 2022 onward.

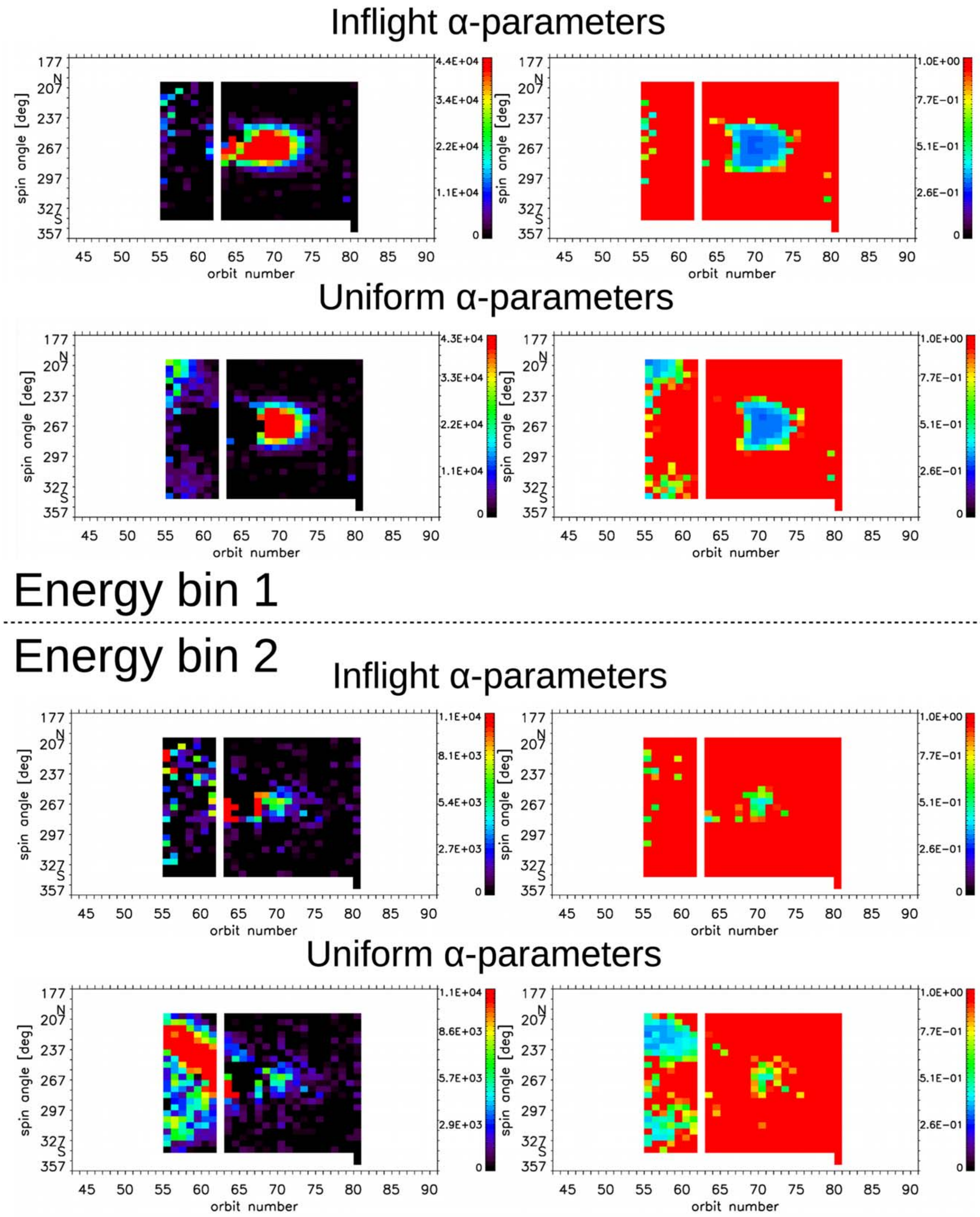

Figure 4. ISN H maps for season 2009–2010 in energy bin 1 (two top rows) and bin 2 (two bottom rows) derived with the in-flight approach (first and third row) vs. the approach with $\alpha \equiv 1$ everywhere (second and fourth row). The left column shows the derived ISN H intensity, the right column shows the corresponding relative uncertainties of the ISN H intensities (red pixels indicate places where the relative uncertainty exceeds 1, i.e., the ISN H intensity is ill constrained). The in-flight α-parameter data and uncertainties for both energy bins is available in a text file as data behind the figure. The data includes 15 yr of maps.

(The data used to create this figure are available in the online article.)

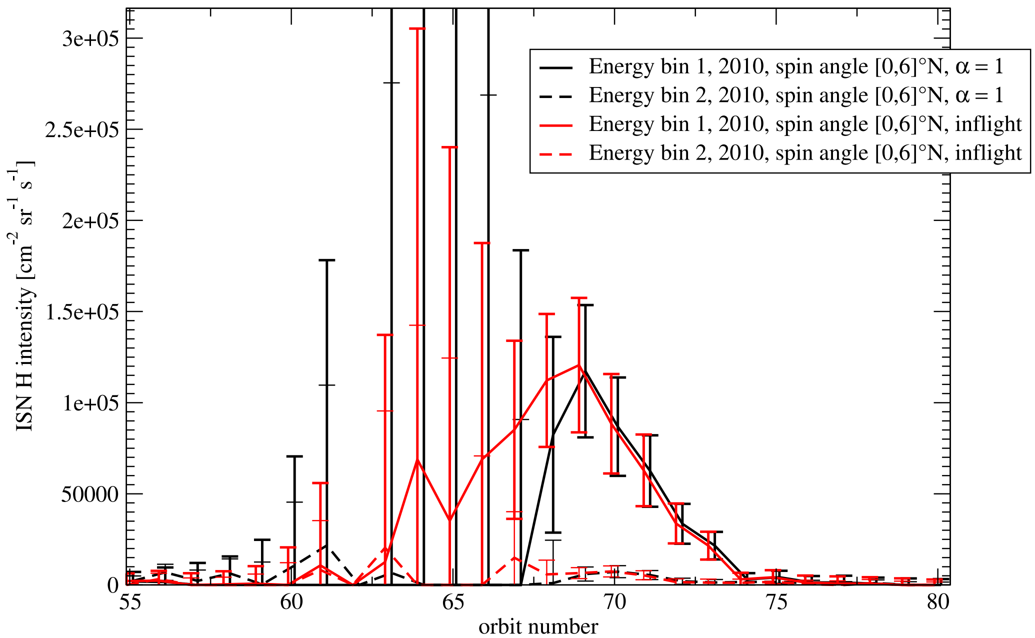

Figure 5. Comparison of algorithms for season 2009–2010: Longitudinal cross section of derived ISN intensities along maximum intensities close to ecliptic plane. Red symbols denote results from the in-flight approach, black symbols show results from the approach with $\alpha \equiv 1$.

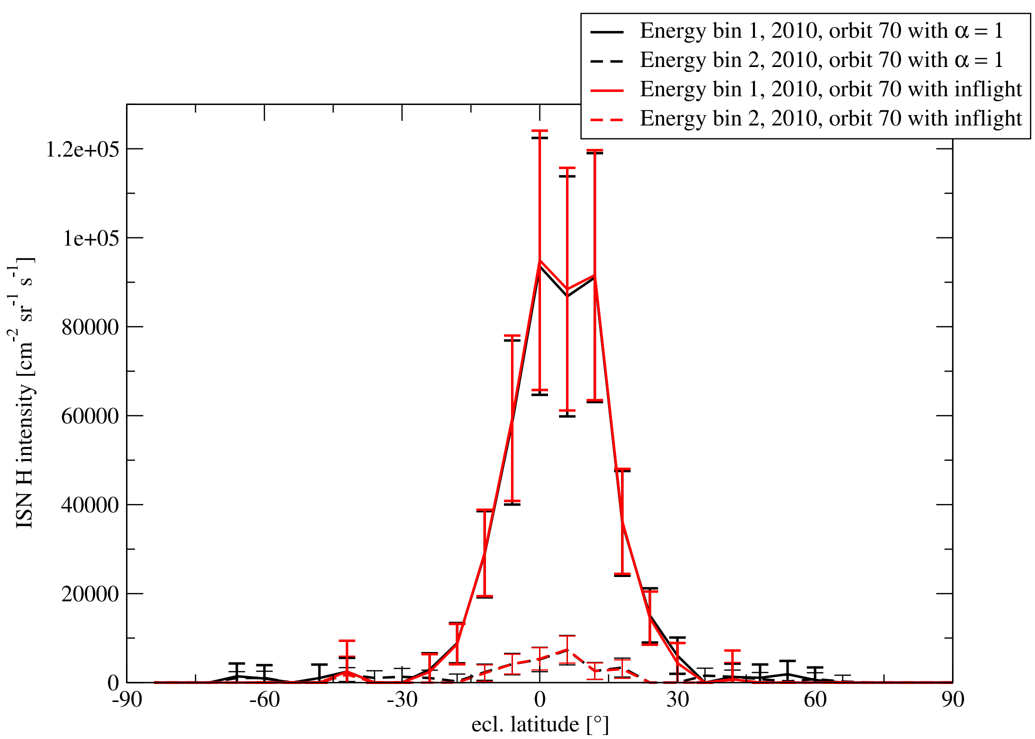

Figure 6. Comparison of algorithms for season 2009–2010: Latitudinal cross section of derived ISN intensities. Red symbols denote results from the in-flight approach, black symbols show results from the approach with $\alpha \equiv 1$.

4.3. Lower than Predicted Energy of ISN H

Heliosphere models predict equal or higher count rates for IBEX-Lo energy bin 2 compared with energy bin 1 for canonical parameters for radiation pressure and ionization rate (O. A. Katushkina et al. 2015, 2021; F. Rahmanifard et al. 2019). The energy of ISN H entering IBEX-Lo for ram observations in the ecliptic plane during low solar activity is expected to be 20–21 eV, i.e., exactly at the limit between energy bin 1 and 2. Based on calibration, fluxes that are twice as high would therefore be expected in energy bin 1 compared to energy bin 2 for the orbits of maximum ISN H signal at low solar activity. However, the ratio of observed ISN H fluxes in energy bin 1 divided by those in energy bin 2 is calculated to 16.8, 18.0, 16.2, 4.0, 5.3, 2.1, 2.3, 7.1, and 7.7 for the years 2009–2018 without 2016, according to A. Galli et al. (2019).

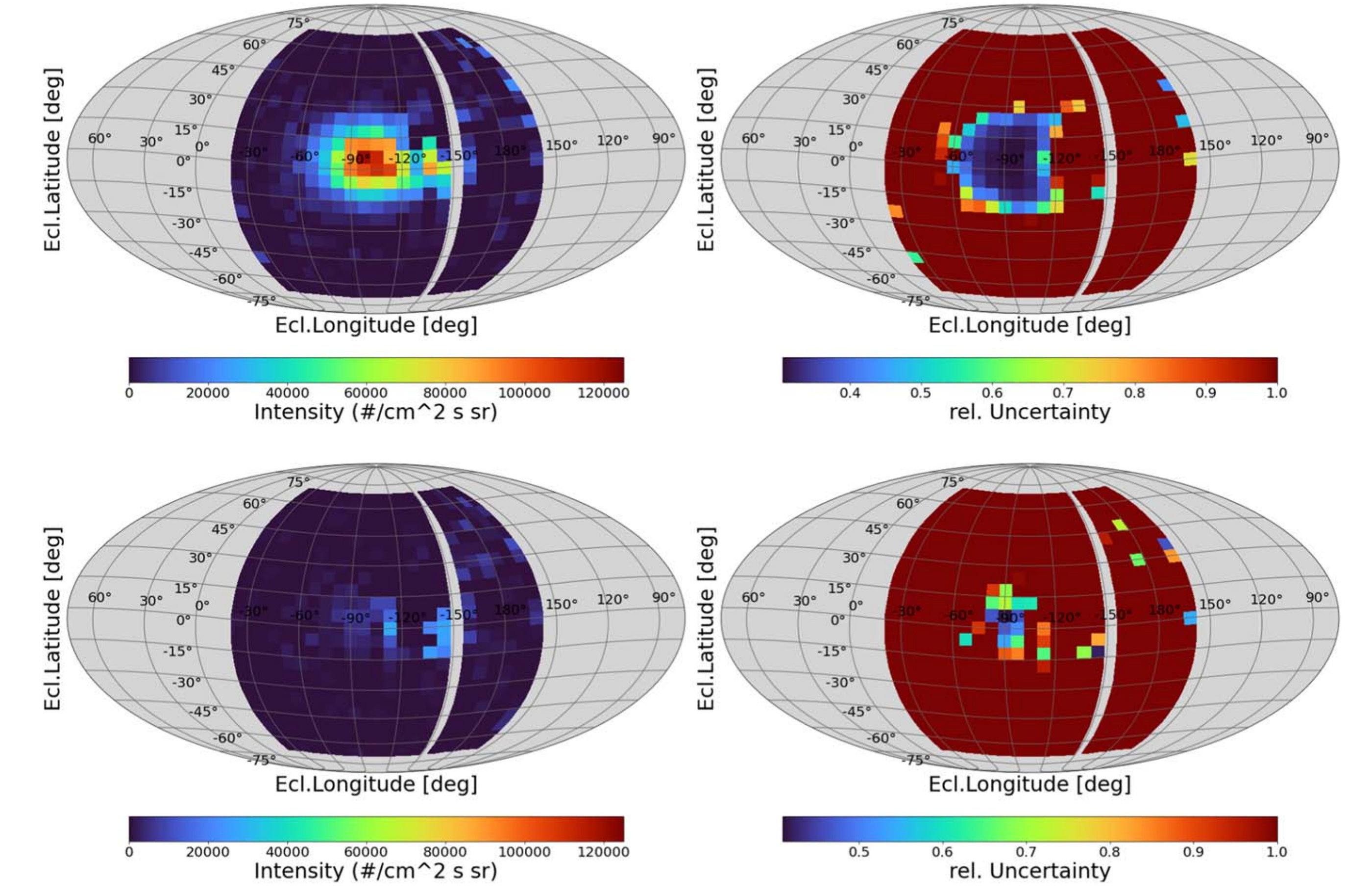

Figure 7. ISN H Mollweide maps in ecliptic coordinates for the ISN season 2009–2010 for energy bins 1 (top row) and 2 (bottom row). The left column shows the derived ISN H intensity, the right column shows the corresponding relative uncertainties of the ISN H intensities.

The high count rates in the lowest energy bin compared with energy bin 2 are also reproduced with the new α-parameters and over two solar minima. This is illustrated in Figure 11. It shows, in the top panel, the time series of ISN H flux in units of $cm^{-2}\,s^{-1}$ over all 15 yr. The bottom panel shows the sunspot numbers as a proxy for solar activity (SILSO World Data Center 2024). There is the obvious and expected anticorrelation of ISN H fluxes in energy bin 1 (red data points) with solar activity (L. Saul et al. 2013; A. Galli et al. 2019). To create the fluxes in Figure 11 from the annual ISN H maps, we summed the intensity of all pixels between ecliptic longitude 225° and 360° with a retrieved intensity $J > 0$ and a relative uncertainty $\sigma_J/J < 1$ and multiplied the sum by the solid angle of the IBEX-Lo instantaneous FOV of $6\overset{\circ}{.}5 \times 6\overset{\circ}{.}5$ (S. A. Fuselier et al. 2009b). This is the same approach as in Figure 13 of A. Galli et al. (2019) except for the modified directional limits: The longitude restriction was chosen to exclude the sparse outlier pixels affected by the prime ISN He at ecliptic longitudes below 225°. Annual entries of energy bin 2 with less than 20 valid map pixels were omitted. The year 2016 had to be omitted for both energy bins because of missing data. The uncertainty of these annual ISN fluxes were calculated with error propagation from the individual uncertainties of all included map pixels in Figures 8–10. For solar minimum conditions around 2009 and 2020, the observed ratio of ISN H fluxes in energy bin 1 compared to bin 2 is between 20 and 30 and 10 ± 2, respectively. The high abundance of ISN H at the lowest energy bin by 1 order of magnitude (with respect to model predictions) thus is confirmed for two solar minima. This discrepancy is not notably affected by the ISN He instrument response assumptions.

The discrepancy of measured and predicted ISN H energies could be caused by shortcomings of heliosphere models (e.g., inaccurate assumptions on ionization rates and radiation pressure) and/or by an offset in instrument calibration. More specifically, the ISN H atoms lose at least 5 eV ($\sim$25%) more than expected, somewhere on their travel from the LISM across the heliosphere boundary regions, through the heliosphere to 1 au, or inside the instrument. Alternatively, the energy acceptance range of IBEX-Lo bin 2 in flight could be shifted to 25–45 eV in contrast to the nominal 20–41 eV FWHM energy range (S. A. Fuselier et al. 2009b), but there is no evidence for this hypothesis. A mere offset of geometric factor $G(21)$ relative to $G(22)$ is unlikely to explain the discrepancy because such an offset would have to be an order of magnitude between neighboring energy bins. Moreover, the spatial distribution of the uncertainty of the retrieved ISN H in energy bin 2 indicates that the ISN H signal at higher energies is indeed at the limit of detectability in most seasons. As a consequence, the ISN H maps in energy bin 2 have, on their own, too few valid pixels and a signal-to-noise ratio too low to serve as a model constraint over the full solar cycle.

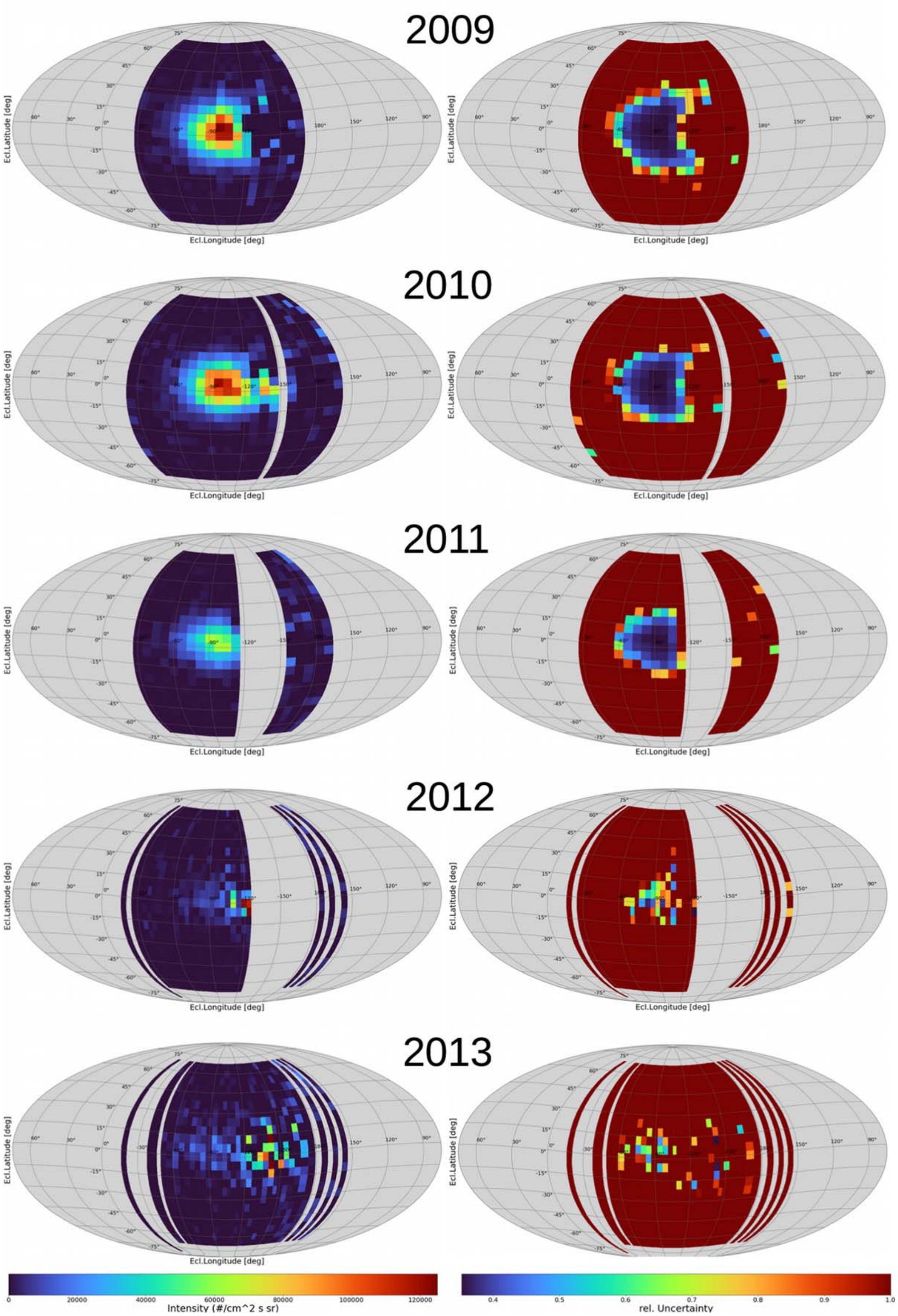

Figure 8. ISN H Mollweide maps in ecliptic coordinates for the ISN seasons 2009–2013 in energy bin 1. The left column shows the derived ISN H intensity in $cm^{-2}\,sr^{-1}\,s^{-1}$ (identical color scale for all years), and the right column shows the corresponding relative uncertainties whereby red pixels indicate a relative uncertainty >1. These ISN H Mollweide maps and uncertainties are available as data behind the figure.

(The data used to create this figure are available in the online article.)

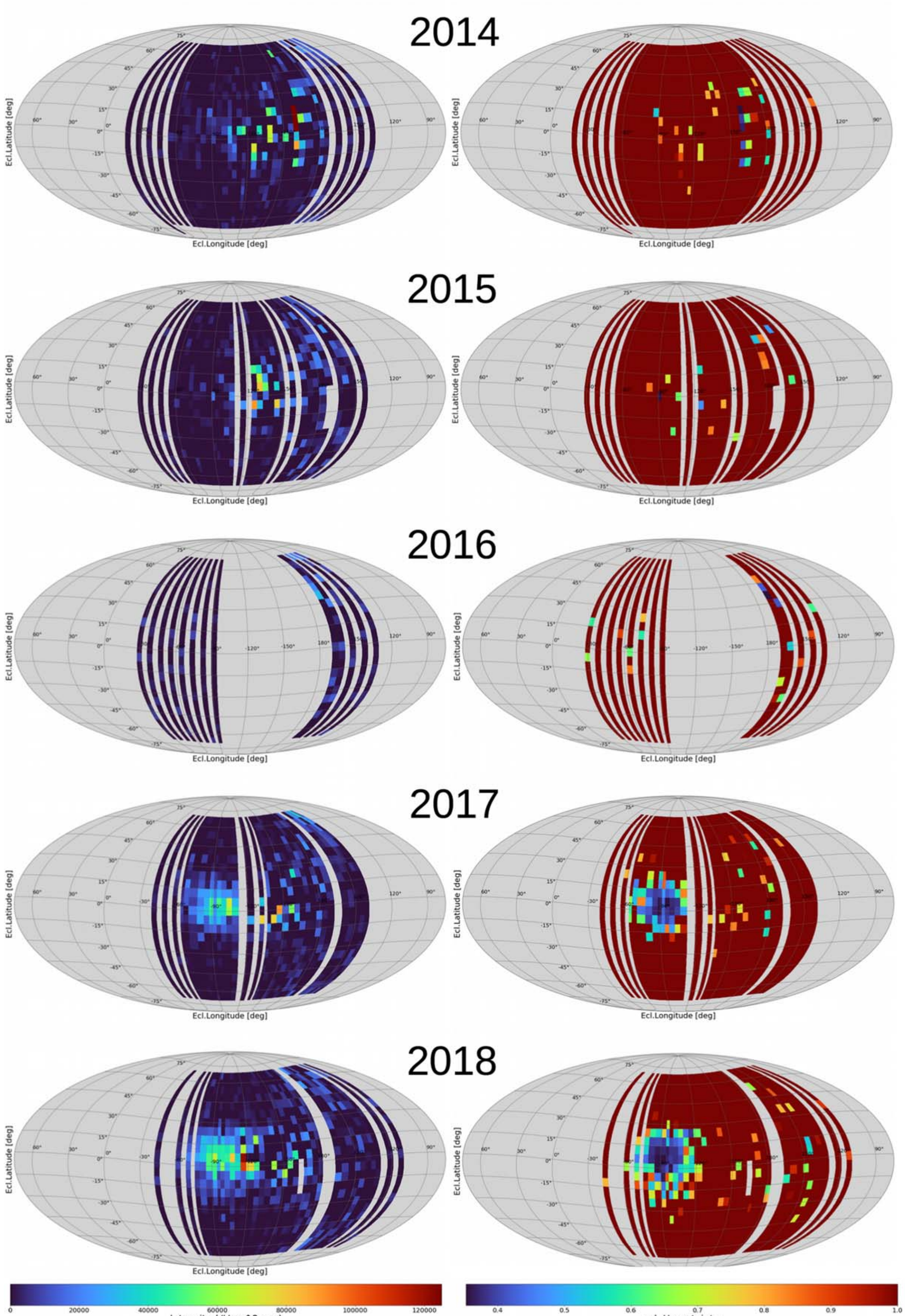

Figure 9. ISN H Mollweide maps in ecliptic coordinates for the ISN seasons 2014–2018 in energy bin 1. The left column shows the derived ISN H intensity in $cm^{-2}\,sr^{-1}\,s^{-1}$ (identical color scale for all years), and the right column shows the corresponding relative uncertainties whereby red pixels indicate a relative uncertainty >1. These ISN H Mollweide maps and uncertainties are available as data behind the figure.

(The data used to create this figure are available in the online article.)

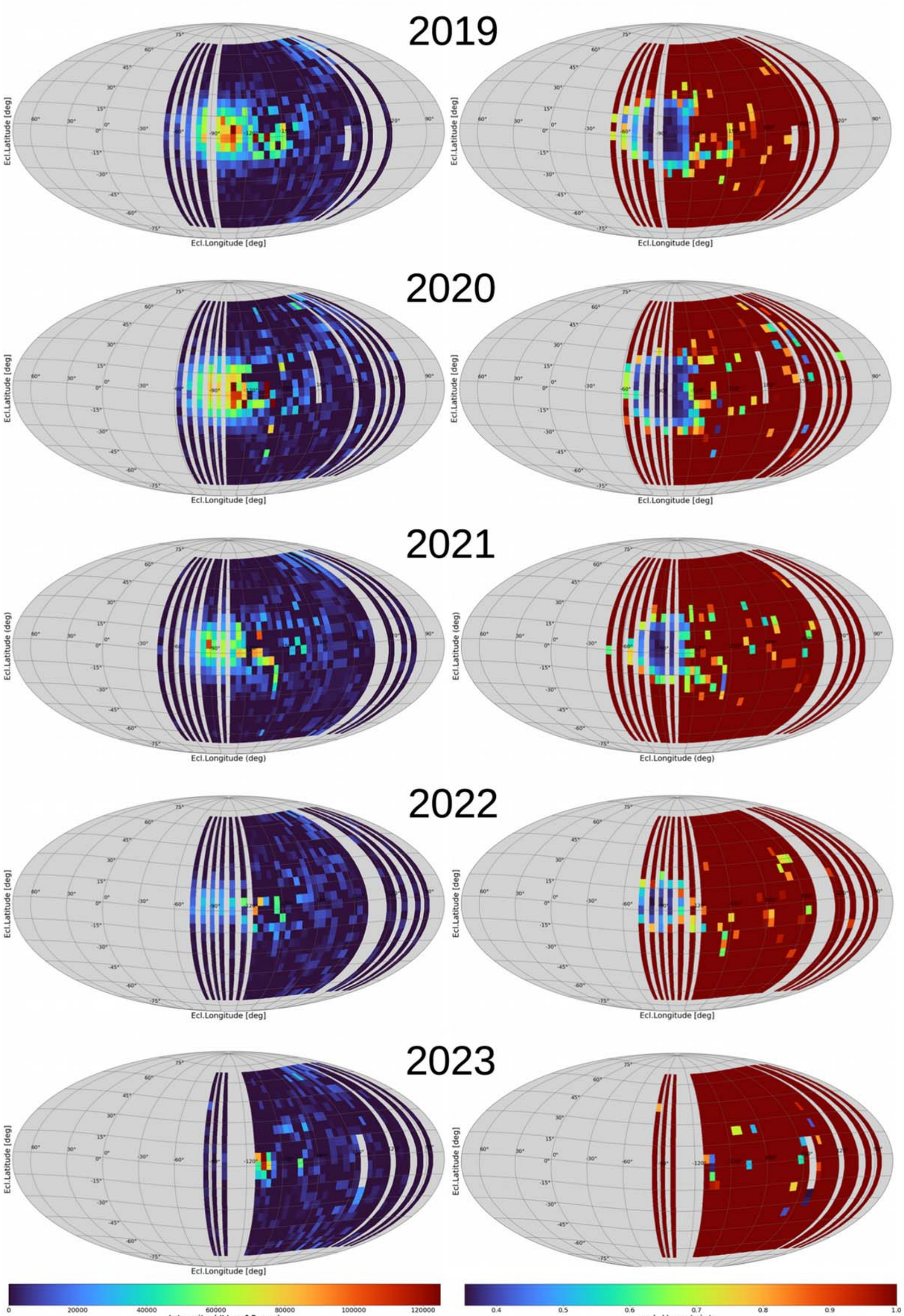

Figure 10. ISN H Mollweide maps in ecliptic coordinates for the ISN seasons 2019–2023 in energy bin 1. The left column shows the derived ISN H intensity in cm^{-2} sr^{-1} s^{-1} (identical color scale for all years), and the right column shows the corresponding relative uncertainties whereby red pixels indicate a relative uncertainty >1. These ISN H Mollweide maps and uncertainties are available as data behind the figure.

(The data used to create this figure are available in the online article.)

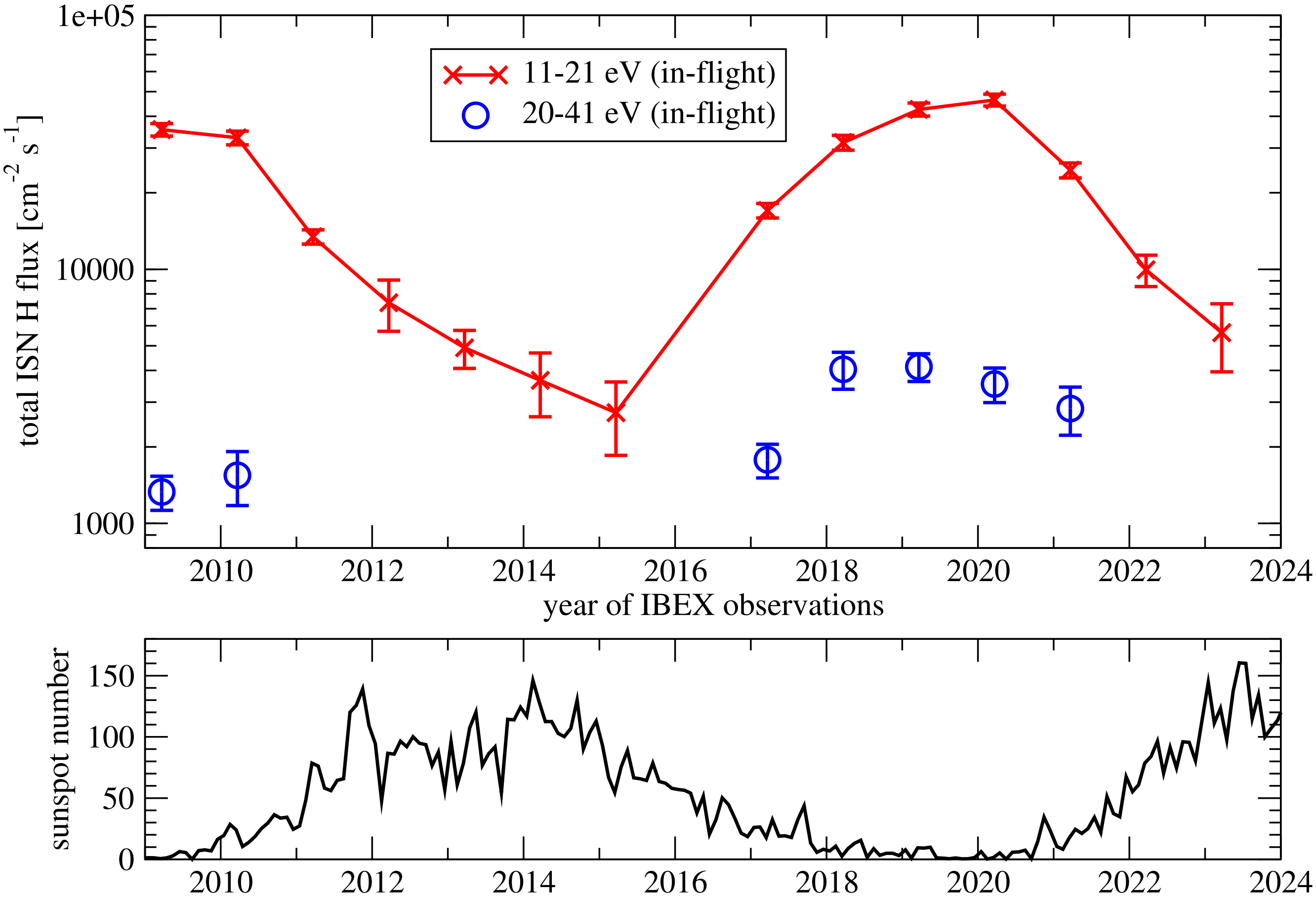

Figure 11. Time series of ISN H flux (top) and solar activity (bottom). The top panel shows the total flux of ISN H in cm^{-2} s^{-1} between 11 and 21 eV (red data points) and between 20 and 41 eV (blue data points) for the year of observation. The data points of 2016 had to be skipped because only a fraction of the potential ISN H signal was covered. The bottom panel shows the number of sunspots as a proxy for solar activity (SILSO World Data Center 2024).

5. Conclusions

This study has presented improved maps of ISN H measured with IBEX-Lo, including additional years and a second solar minimum not covered before. The ISN H signal at energies below 40 eV has been retrieved from the much more intense ISN He signal with appropriate knowledge of the instrument calibration, choice of optimum observation season, and supporting modeling. These new ISN H maps will be the basis for more detailed future interpretation with quantitative comparison to heliosphere models and to other heliospheric data sets (e.g., from Voyager and New Horizons) to better constrain H trajectories and hence heliospheric processes such as radiation pressure.

The temporal variability of the total ISN H flux at 1 au reacts as expected to changes in solar activity, i.e., the most intense signal is observed during solar minima. The absolute flux at the beginning and end of solar cycle 24 is the same within 50%. On the other hand, the energy discrepancy established for shorter IBEX data sets persists: the ISN H atoms reaching IBEX at 1 au appear to have lower energies than predicted with heliosphere models.

The main challenges of identifying the ISN H signal throughout the solar cycle are the weakness of the signal during high solar activity and the partial overlap with the much more intense ISN He signal. The successor instrument of IBEX-Lo on the Interstellar Mapping and Acceleration Probe (IMAP), IMAP-Lo (D. J. McComas et al. 2018), will improve the separation of ISN H and He signals in time and space thanks to the unique capability of the IMAP-Lo instrument to pivot the boresight vector of the instrument during the annual orbit of IMAP (M. A. Kubiak et al. 2024).

Acknowledgments

We thank all of the outstanding people who have made the IBEX mission such a wonderful success. N.A.S., E.M., S.A.F., and D.J.M. are all funded by the IBEX mission as part of NASA's Explorer Program (80NSSC18K0237). J.M.S. and J.G. are funded by NASA's Explorer Program 80NSSC20K0719. P. S. is supported by a project cofinanced by the Polish National Agency for Academic Exchange within the Polish Returns Programme (BPN/PPO/2022/1/00017), with a research component funded by the National Science Centre, Poland (2023/02/1/ST9/00004). M.B. and M.A.K. are supported by a Polish National Science Centre grant 2023/51/BST9/01921. This paper has benefited from the International Space Science Institute (ISSI) in Bern, through ISSI International Team project #541 (Distribution of Interstellar Neutral Hydrogen in the Sun's Neighborhood).

Conflict of Interest

The authors declare that they have no conflict of interest.

ORCID iDs

André Galli https://orcid.org/0000-0003-2425-3793
Paweł Swaczyna https://orcid.org/0000-0002-9033-0809
Maciej Bzowski https://orcid.org/0000-0003-3957-2359
Marzena A. Kubiak https://orcid.org/0000-0002-5204-9645
Izabela Kowalska-Leszczynska https://orcid.org/0000-0002-6569-3800
Peter Wurz https://orcid.org/0000-0002-2603-1169
Fatemeh Rahmanifard https://orcid.org/0000-0001-9316-0553
Nathan A. Schwadron https://orcid.org/0000-0002-3737-9283
Stephen A. Fuselier https://orcid.org/0000-0003-4101-7901
Justyna M. Sokół https://orcid.org/0000-0002-4173-3601
Jacob Heerikhuisen https://orcid.org/0000-0001-7867-3633
David J. McComas https://orcid.org/0000-0001-6160-1158

References

Bochsler, P., Petersen, L., Möbius, E., et al. 2012, ApJS, 198, 13
Bzowski, M., Czechowski, A., Frisch, P. C., et al. 2019, ApJ, 882, 60
Bzowski, M., Fahr, H. J., Rucinski, D., & Scherer, H. 1997, A&A, 326, 396
Bzowski, M., Kubiak, M. A., Czechowski, A., & Grygorczuk, J. 2017, ApJ, 845, 15
Fraternale, F., Pogorelov, N. V., & Heerikhuisen, J. 2021, ApJL, 921, L24
Funsten, H. O., Allegrini, F., Bochsler, P., et al. 2009a, SSRv, 146, 75
Funsten, H. O., Allegrini, F., Crew, G. B., et al. 2009b, Sci, 326, 964
Fuselier, S. A., Allegrini, F., Funsten, H. O., et al. 2009a, Sci, 326, 962
Fuselier, S. A., Bochsler, P., Chornay, D., et al. 2009b, SSRv, 146, 117
Galli, A., Baliukin, I. I., Bzowski, M., et al. 2022a, SSRv, 218, 31
Galli, A., Wurz, P., Fuselier, S. A., et al. 2014, ApJ, 796, 9
Galli, A., Wurz, P., Park, J., et al. 2015, ApJS, 220, 30
Galli, A., Wurz, P., Rahmanifard, F., et al. 2019, ApJ, 871, 52
Galli, A., Wurz, P., Schwadron, N. A., et al. 2017, ApJ, 851, 2
Galli, A., Wurz, P., Schwadron, N. A., et al. 2022b, ApJS, 261, 18
Heerikhuisen, J., Zirnstein, E. J., Pogorelov, N. V., Zank, G. P., & Desai, M. 2019, ApJ, 874, 76
Katushkina, O. A., Galli, A., Izmodenov, V. V., & Alexashov, D. B. 2021, MNRAS, 501, 1633
Katushkina, O. A., Izmodenov, V. V., Alexashov, D. B., Schwadron, N. A., & McComas, D. J. 2015, ApJS, 220, 33
Kubiak, M. A., Bzowski, M., Möbius, E., & Schwadron, N. A. 2024, ApJS, 271, 43
Kubiak, M. A., Bzowski, M., Sokøł, J. M., et al. 2014, ApJS, 213, 29
McComas, D. J., Alimaganbetov, M., Beesley, L. J., et al. 2024, ApJS, 270, 17
McComas, D. J., Allegrini, F., Bochsler, P., et al. 2009, Sci, 326, 959
McComas, D. J., Bzowski, M., Fuselier, S. A., et al. 2015, ApJS, 220, 22
McComas, D. J., Carrico, J. P., Hautamaki, B., et al. 2011, SpWea, 9, S11002
McComas, D. J., Christian, E. R., Schwadron, N. A., et al. 2018, SSRv, 214, 116
Möbius, E., Bochsler, P., Bzowski, M., et al. 2009, Sci, 326, 969
Möbius, E., Bochsler, P., Bzowski, M., et al. 2012, ApJS, 198, 11
Park, J., Kucharek, H., Paschalidis, N., et al. 2019, ApJ, 880, 4
Rahmanifard, F., Möbius, E., Schwadron, N. A., et al. 2019, ApJ, 887, 217
Rodríguez Moreno, D. F., Wurz, P., Saul, L., et al. 2013, A&A, 557, A125
Saul, L., Bzowski, M., Fuselier, S. A., et al. 2013, ApJ, 767, 130
Schwadron, N. A., Bzowski, M., Crew, G. B., et al. 2009, Sci, 326, 966
Schwadron, N. A., Möbius, E., Kucharek, H., et al. 2013, ApJ, 775, 86
SILSO World Data Center 2024, International Sunspot Number Monthly Bulletin and Online Catalogue, www.sidc.be/SILSO/home
Sokół, J. M., Kubiak, M. A., & Bzowski, M. 2019, ApJ, 879, 24
Swaczyna, P., Bzowski, M., Fuselier, S., et al. 2023, ApJS, 266, 2
Swaczyna, P., Bzowski, M., Kubiak, M. A., et al. 2015, ApJS, 220, 26
Zirnstein, E. J., Heerikhuisen, J., Funsten, H. O., et al. 2016, ApJL, 818, L18